Catalysis
Science & Technology

Cite this: *Catal. Sci. Technol.*, 2012, **2**, 2361–2366

www.rsc.org/catalysis

PAPER

$CoFe_2O_4$–ZnS nanocomposite: a magnetically recyclable photocatalyst†

Kula Kamal Senapati, Chandan Borgohain and Prodeep Phukan*

Received 11th June 2012, Accepted 18th June 2012
DOI: 10.1039/c2cy20400b

A new synthesis of a $CoFe_2O_4$–ZnS magnetic nanocomposite has been achieved and used as an efficient photocatalyst in the degradation of methyl orange in water under UV irradiation. The photocatalyst is magnetically recoverable from the reaction medium and suitable for multiple uses with sustained catalytic activity.

Introduction

Magnetic nanocomposites (NCs) are gaining importance in recent years for their potential applications in varied fields of fundamental science and technology such as biomedical engineering, chemical sensing, magneto-optical devices, solar cells and catalysis.[1,2] These hybrid structures have been extensively investigated because they can provide the combined advantages of the constituent materials relative to their single-component counterparts. They exhibit improved chemical and physical properties such as thermal and chemical stability, better solubility, less or no cytotoxicity, *etc*.

Semiconductor nanocatalysts having high surface area, strong UV absorption and long life-span have been widely used for the degradation of organic pollutants in water.[3–5] Among these, ZnS (bandgap energy: 3.6–3.8 eV) has served as one of the most efficient photocatalysts for wastewater treatment such as in the photodegradation of dyes, *p*-nitrophenol, and halogenated benzene derivatives, reduction of heavy metals and water-splitting for H_2 evolution.[6–11] Recently, Suslick developed a nanostructured Ni^{2+}-doped ZnS photocatalyst for the evolution of H_2 under visible light.[12] ZnS nanoparticles (NPs) are a good photocatalyst due to the rapid generation of electron–hole (e−/h+) pairs by photoexcitation and high negative reduction potentials of excited electrons. However, they have the serious limitation of easy recombination of e−/h+ pairs which in turn reduce the photocatalytic activity significantly.[13,14] Moreover, these types of suspended photocatalysts suffer a noticeable disadvantage in ease of separation, recovery, recycling and high cost in large scale production.[15] In addition, they tend to agglomerate in aqueous solution and hinder the penetration of lights.

Consequently, design and development of magnetic NCs with high catalytic activity and easy separation can heighten their potential for practical applications. Magnetic materials such as Fe_3O_4,[16,17] $BaFe_2O_4$,[18,19] $NiFe_2O_4$[20,21] and γ-Fe_2O_3[22] have recently been utilized as core materials in making magnetic NCs with TiO_2 or ZnO semiconductor shells, which can be easily separated from a solution by applying a magnetic field.

It is also noteworthy that the fabrication of a magnetic-nanocomposite with a uniform coating over the core surface in nano-scale dimensions is a challenging task due to difficulties in complete dispersion of the magnetic core in solution. Moreover, the commonly used core materials such as Fe_3O_4 or γ-Fe_2O_3 are not chemically or thermally stable.[23] Therefore, a new approach for preparing a stable and highly dispersible magnetic core is desirable for effective coating with catalytically active species in nano-scale dimensions.

Recently, we have reported a new magnetic nanocomposite using ferromagnetic $CoFe_2O_4$ as the core material with multi-functional properties.[24–27] $CoFe_2O_4$ is well-known to have large magnetic anisotropy, moderate saturation magnetization, remarkable chemical stability and mechanical hardness,[28] which makes it a good candidate as a core material for the fabrication of NCs. Zhang reported a new $CoFe_2O_4$-ZnO nanocomposite with multiple properties.[29] Very recently, Mourão reported the synthesis of a $CoFe_2O_4$-TiO_2 nanocomposite for photodegradation of dye in water.[30] The photocatalytic activity of these NCs might be related to the electronic and absorption properties of the core materials which could restrain the recombination of e−/h+ pairs by absorbing photo-generated electrons from the conduction band of the semiconductor. Thus, the avenue of $CoFe_2O_4$ as a core material can be explored for the development of a conjugate of $CoFe_2O_4$ and ZnS NPs. However, no study on photocatalytic activity of $CoFe_2O_4$–ZnS NCs has been reported so far. Therefore, a study on such conjugates might pave the way for developing recyclable photocatalysts for the degradation of organic contaminants in water and environmental remediation.

2. Experimental section

2.1 Synthesis of $CoFe_2O_4$–ZnS nanocomposite

Initially, a magnetic core of $CoFe_2O_4$ NPs was prepared by ultrasonication-assisted co-precipitation and then a layer of

Department of Chemistry, Gauhati University, Guwahati-781014, Assam, India. Fax: (+)91-361-2700311; E-mail: pphukan@yahoo.com

† Electronic supplementary information (ESI) available. See DOI: 10.1039/c2cy20400b

ZnS NPs was structured over it forming the $CoFe_2O_4$–ZnS nanocomposite. The $CoFe_2O_4$ magnetic core was synthesized following our previously reported method[24,25] except a 1 : 1 adduct of oleic acid-dodecylamine was used for higher stability and better compatibility with ZnS. Then, ZnS NPs were prepared by a modified method reported by Saravanan *et al.*[31] and added in to the dispersion of $CoFe_2O_4$ NPs in ethanol to obtain $CoFe_2O_4$–ZnS core-shell NCs ($CoFe_2O_4$–ZnS NCs). The detail of the synthetic protocol is described in the supplementary information.†

2.2. Characterization

The X-ray diffraction (XRD) patterns of the as-synthesized samples were measured using an X-ray diffractometer (Bruker AXS D8) with Cu-Kα radiation (λ = 1.54178 Å) and a graphite monochromator from 20° to 70° (2θ) at a scanning rate of 5° min^{-1}. The particle size and morphology of the samples were characterized by transmission electron microscopy (TEM, JEOL JEM2100) using an accelerating voltage of 200 kV with the potential of performing selected area electron diffraction (SAED). Field emission scanning electron microscopy (FESEM, Carl Zeiss, ΣIGMA) was also performed to observe the surface morphology of the samples. For TEM measurement, a drop of a dispersion of the NPs in ethanol was placed on a carbon coated copper grid (400 mesh size) and evaporated to dryness. The absorption spectra of methyl orange (MO) solutions were obtained by a UV-Vis spectrophotometer (Varian, Cary 50). The Raman spectra of the samples were recorded using a 633 nm line of He-Ne laser as the excitation source in a Laser Micro-Raman Spectrometer (HORIBA Jobin Yvon, Lab RAM HR) at room temperature. The magnetic properties of the $CoFe_2O_4$–ZnS NCs and $CoFe_2O_4$ NPs were measured in a vibrating sample magnetometer (VSM, Lakeshore 7410) with a maximum applied field of ±2 T. The specific surface area and porosity were measured by the application of the Brunauer-Emmett-Teller (BET) equation and the Barrett-Joyner-Halanda (BJH) method.[32] The sample was first degassed for 2h at 200 °C and then analyzed by a Backman Coulter (SA 3100) Surface Area and Pore Size Analyzer. Liquid chromatography–mass spectrometry (LCMS, Waters, Q-Tof Premier LCMS) analysis was performed to observe the degradation products of MO.

2.3. Photocatalytic activity measurement

The photocatalytic activities of the as-synthesized samples were measured on degradation of MO in aqueous medium under UV illumination at different time intervals. The samples (0.02 g of each) of $CoFe_2O_4$–ZnS, ZnS and $CoFe_2O_4$ NPs were placed separately into a 200 mL tubular quartz vessel containing 100 mL of 1×10^{-5} M MO aqueous solutions and mixed by ultrasonication for 10 min. Then, the mixtures were stirred in the dark (30 min) to obtain adsorption–desorption equilibrium until the concentration of MO was constant. The mixtures were then illuminated with a UV lamp (12 mW, main wavelength of 400 nm), and were put into the bottom of the quartz vessel and stirred continuously. All experiments were carried out at ambient temperature (25 °C) with circulation of water through the outer jacket of the reaction vessel. During the course of the reaction, the mixtures were sampled at different times and separated by a magnet to discard any residue. Then, an absorption spectrum of each sample was recorded through a wavelength scan from 300 to 600 nm on a UV-Vis spectrophotometer. The characteristic absorption of MO at 460 nm was chosen as the monitoring parameter for the photocatalytic degradation process. The photocatalytic degradation percentage of MO was calculated using eqn (1)

$$\text{Degradation}(\%) = \left(\frac{A_0 - A}{A_0}\right) \times 100 \qquad (1)$$

where A_0 is the initial absorbance of MO before degradation and A is the absorbance after time t.

Results and discussion

In the present article, we report the synthesis and characterization of a core–shell $CoFe_2O_4$–ZnS NC and its photocatalytic property. The composite was found to exhibit excellent performance in photodegadation of MO in water under UV irradiation. To the best of our knowledge, this is a new magnetic NC which has been used for the photodegradation of a dye.

The Powder XRD measurement was done individually for the ZnS, $CoFe_2O_4$ and $CoFe_2O_4$–ZnS NPs to characterize the phase and crystallization (Fig. 1a–c). It can be seen that cubic ZnS NPs (JCPDS card 5-0566)[33] have been prepared and the broadening of diffraction peaks is in accordance with the nanocrystalline nature of the ZnS particles. The diffraction pattern of the as-synthesized $CoFe_2O_4$–ZnS particles (Fig. 1a) shows that all the peaks are in good agreement with the cubic structure of spinel $CoFe_2O_4$ (JCPDS cards: 3-864 and 22-1086)[34,35] and of ZnS NPs. These results reveal that the nanocomposite is composed of cubic-structured $CoFe_2O_4$ and ZnS NPs. The average size of the crystalline particles for the primary $CoFe_2O_4$ NPs and ZnS NPs was estimated to be 30 ± 2 nm and 7 ± 1 nm, respectively, based on the Debye–Scherrer formula.[36]

Fig. 2 shows the representative TEM image, with the SAED pattern in the inset, of the as-prepared ZnS NPs showing the uniform size-distribution with the size in between 5–10 nm, which is in good agreement with the size determined from the Debye–Scherrer relation.[36] The diffraction rings have been identified as the (111), (220) and (311) planes of the cubic ZnS phase.[33] The morphology of the $CoFe_2O_4$–ZnS NCs was analyzed by FESEM (Fig. S1 in ESI†) and TEM measurement as shown in Fig. 2 (c, d) which show the uniform size distribution

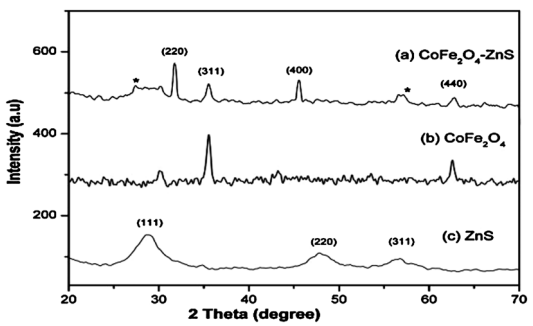

Fig. 1 XRD pattern of (a) $CoFe_2O_4$–ZnS (*contribution from ZnS NPs), (b) $CoFe_2O_4$ and (c) ZnS NPs.

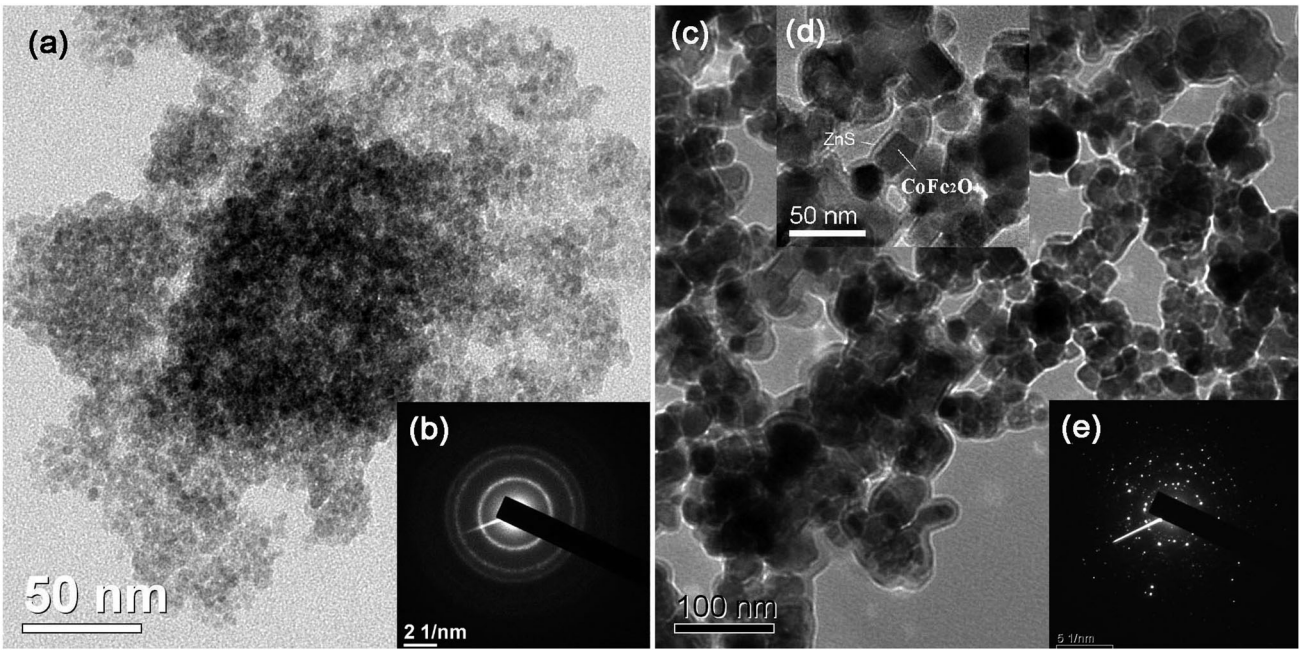

Fig. 2 TEM image of (a) ZnS NPs and (c, d) $CoFe_2O_4$–ZnS NCs with the corresponding SAED patterns (b, e).

of NPs with cubic morphology. The corresponding SAED pattern of the composite is shown in the inset of Fig. 2(e). The crystalline sizes were found to be about 30 ± 5 nm, which were close to the average crystallite size obtained from the Debye–Scherrer formula based on XRD patterns. A close observation of the FESEM micrographs indicates that the primary $CoFe_2O_4$ nanocrystals are covered with ZnS NPs. The TEM image of $CoFe_2O_4$–ZnS NCs shows the core-shell nanostructure, where the dark particles of $CoFe_2O_4$ are shielded by a thin layer of bright ZnS particles (Fig. 2c–d).

The lattice image of the nanocomposite (Fig. S3–S5 of ESI†) marked with the (111) lattice plane of spinel $CoFe_2O_4$ and the (220) lattice plane of cubic ZnS NPs revealed the highly crystalline nature of the NCs. The high resolution TEM (HRTEM) image allowed us, by means of Gatan Digital Micrograph™ software, to obtain the fast Fourier transform (FFT) from which lattice spacings of 4.59 A° and 2.7 A° were obtained (experimental error, <5%) for the $CoFe_2O_4$ and ZnS NPs, respectively.

The as-synthesized NPs were further characterized by laser micro Raman spectroscopy which is a useful tool for investigating NPs and their surrounding media.[37] Strong evidence for the core–shell structure of $CoFe_2O_4$–ZnS NCs was also observed in the Raman spectra. The inset in Fig. 3 shows the Raman spectra of ZnS NPs with the characteristic peaks at around 259 and 345 cm^{-1} which indicates the cubic structure of ZnS NPs.[38] The spinel $CoFe_2O_4$ shows five Raman active modes ($A_g + E_g + 3E_{2g}$).[39] Three modes of $CoFe_2O_4$ NPs at 458 cm^{-1}, 600 cm^{-1} and 665 cm^{-1} can be seen in Fig. 3(b) along with the 258 cm^{-1} and 345 cm^{-1} modes from ZnS NPs. We did not observe any significant shifts in bands of Raman spectra, which indicates that there is no substitution in the $CoFe_2O_4$–ZnS nanocomposite.[40] Therefore, it may be inferred that the core–shell structured $CoFe_2O_4$–ZnS NC has been effectively synthesized.

We further evaluated the magnetic properties of the $CoFe_2O_4$ core and the $CoFe_2O_4$–ZnS NCs by VSM measurement at room

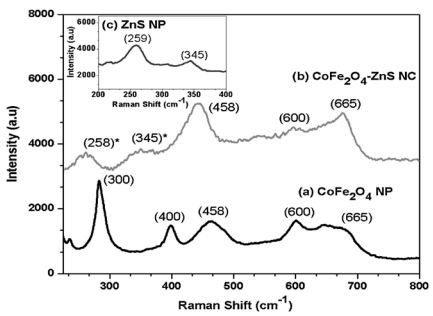

Fig. 3 Raman spectra of (a) $CoFe_2O_4$ NPs and (b) $CoFe_2O_4$–ZnS NCs and the inset is of ZnS NPs (*Raman scattering peaks from ZnS NPs).

temperature as shown in Fig. 4. The NCs give the coercivity (*Hc*) and saturation magnetization (*Ms*) of 1.2 kOe and 17.5 emu g^{-1} respectively which is only a negligible change from the $CoFe_2O_4$ core (*Hc*: 1.6 kOe and *Ms*: 18 emu g^{-1}) and that is an indication of the formation of nano-scale coating at the core-surface. The band-gap energy, E_g of the as-synthesized nanocomposite was determined based on the Tauc plot[41] and was found to be 3.2 eV from the absorbance spectra (Fig. S6 in ESI†).

The specific surface area and porosity were measured by the application of the BET equation and the BJH method. Fig. 5 shows the N_2 adsorption–desorption isotherms of the $CoFe_2O_4$–ZnS NC. The BET surface area of the NCs was found to be 30.269 m^2 g^{-1} as calculated by the linear part of the BET plot, which is much higher than that of the $CoFe_2O_4$ NPs prepared by the co-precipitation method (17.97 m^2 g^{-1}).[42] The total pore volume at P/P_o = 0.98 is 0.18 cm^3 g^{-1}. The BET isotherm is of type II and H3 hysteresis loop (BDDT/IUPAC classification), characteristic of mesoporous adsorbents.[43]

To investigate the potential application of the magnetic NC as a recyclable photocatalyst for the removal of contaminants from wastewater, we performed the degradation of MO in an

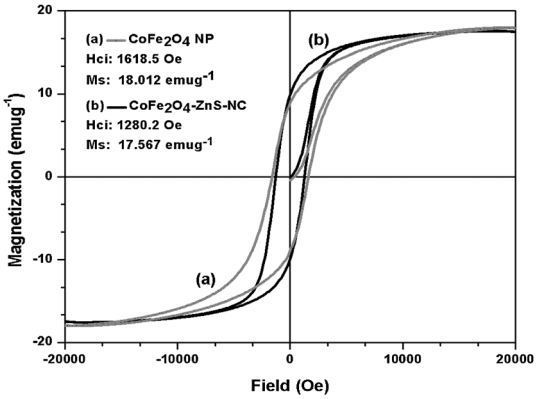

Fig. 4 Magnetic hysteresis loops for (a) $CoFe_2O_4$ NPs and (b) $CoFe_2O_4$–ZnS NCs.

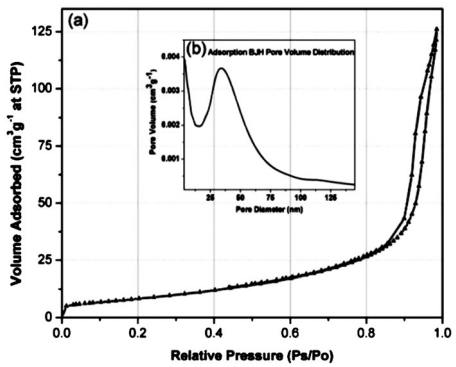

Fig. 5 BET isotherm and pore size distribution (inset) of the as-synthesized $CoFe_2O_4$–ZnS magnetic NPs.

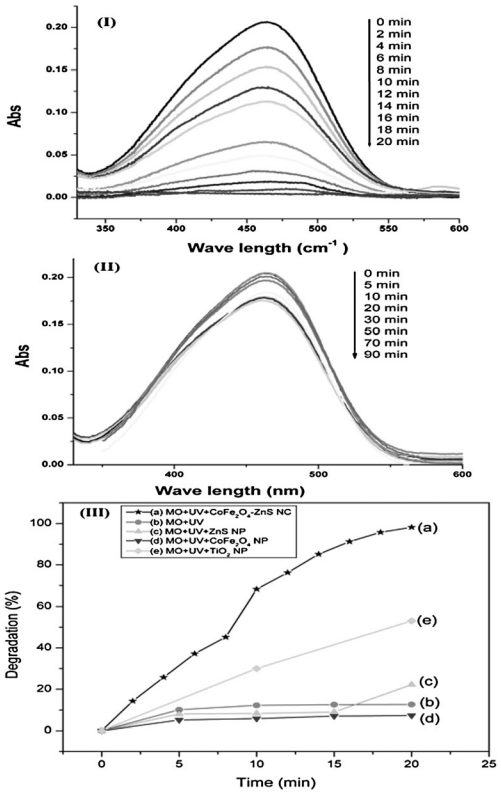

Fig. 6 Changes of UV-Vis spectra of MO with irradiation time in the presence of (I) $CoFe_2O_4$–ZnS NCs and (II) ZnS NPs and (III) degradation curves of MO with (a) $CoFe_2O_4$–ZnS NCs, (b) no catalyst, (c) ZnS NPs, (d) $CoFe_2O_4$ NPs and (e) TiO_2 NPs under UV light irradiation.

aqueous medium driven by UV-irradiation as a probe reaction. Fig. 6 (I) and (II) show the absorption spectra of an aqueous solution of MO irradiated under UV-light for different time intervals in the presence of $CoFe_2O_4$–ZnS NCs and ZnS NPs, respectively. The typical absorption peak at 460 nm gradually disappears as the UV-irradiation time increases, and completely diminishes after 20 min, meaning complete photodegradation of MO by the $CoFe_2O_4$–ZnS NCs. The photocatalytic degradations of MO over different time intervals using the as-synthesized samples as the catalyst and with no catalyst are shown in Fig. 6 (III). We have observed that the $CoFe_2O_4$–ZnS NCs exhibit high photocatalytic efficiency with a degradation of 98% in 20 min of UV light exposure. The photocatalytic degradation of MO was further investigated by LCMS analysis as described in the supplementary information (Fig. S10–13 in ESI†) which revealed its appreciable degradation under the photocatalytic conditions applied. Thus, a NC with enhanced photocatalytic activity has been achieved that is capable of faster degradation of MO than any other reported method.[44–46]

For comparison, we also checked the photocatalytic activity of the as-synthesized $CoFe_2O_4$ core and ZnS NPs shell employing entirely the same photocatalytic conditions. While keeping all the reaction conditions the same, the ZnS NPs showed low photocatalytic activity and no apparent photocatalytic activity was also detected for $CoFe_2O_4$ NPs under the identical UV-irradiation. We also tested the photocatalytic activity of TiO_2 NPs (TEM and XRD are shown in Fig. S7 and S8, respectively, in ESI†) under the same reaction conditions and observed very low degradation of MO in 20 min of UV light exposure. The good photocatalytic activity of the $CoFe_2O_4$–ZnS NCs with a larger rate (rate constant: 0.0718 min^{-1}) in spite of much larger particle sizes as compared to ZnS NPs, which have considerably low photocatalytic activity (rate constant: 0.0041 min^{-1}), may be associated with small crystallites and poor crystallinity of small NPs. In addition, the high photocatalytic efficiency of the NCs as compared to ZnS NPs is due to the electrostatic interaction between the core and shell components of the conjugate nanostructure of $CoFe_2O_4$ and ZnS NPs.

The corresponding mechanism can be interpreted as follows: under UV light irradiation, electrons in the valence band (VB) of ZnS are excited to its conduction band (CB) leaving the same amount of holes in the VB forming the $e-/h+$ pairs. Due to the strong interfacial connection between ZnS and $CoFe_2O_4$, the excited electrons of the CB of ZnS can transfer to that of $CoFe_2O_4$. So, the $e-/h+$ pairs are separated at the $CoFe_2O_4$–ZnS interfaces, which decreased their recombination probability. Meanwhile, the O_2 absorbed on the $CoFe_2O_4$ surface can accept electrons and enhance the efficiency of generating hydroxyl radicals, which are very reactive towards the degradation of organic molecules and so enhanced photocatalytic activity is observed. A plausible mechanistic scheme of the charge separation and the photocatalytic activity for the photocatalyst is shown in Scheme 1.

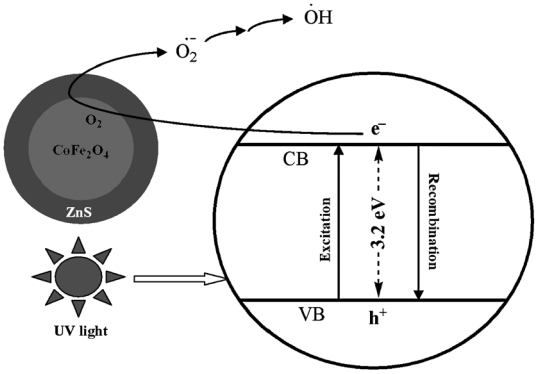

Scheme 1 Illustration of photocatalysis by $CoFe_2O_4$–ZnS NCs.

The photocatalytic decomposition of MO by $CoFe_2O_4$–ZnS NCs follow a pseudo first-order kinetic law, and can be expressed as

$$-\ln\left(\frac{C}{C_o}\right) = kt, \qquad (2)$$

where C and C_o are the reactant concentration at time $t = t$ and $t = 0$, respectively, and k and t are the pseudo-first order rate constant and time respectively.[47] The relationships between $\ln(C_o/C)$ and irradiation time (t) for both the $CoFe_2O_4$–ZnS and ZnS samples are shown in Fig. 7.

It can be seen that there exists a linear relationship between $\ln(C_o/C)$ and irradiation time. The pseudo-first-order rate constant and linear regression coefficients (R) for photodegradation of MO with $CoFe_2O_4$–ZnS NCs and ZnS NPs are mentioned in the graph. It has been observed that the photodegradation rate by $CoFe_2O_4$–ZnS NCs ($k = 0.0718$ min^{-1}) is much faster than that by ZnS NPs ($k = 0.0041$ min^{-1}).

To extend the scope of the nanocomposite for photodegradation of other dyes, we checked the degradation of methylene blue and phenolphthalein using the $CoFe_2O_4$–ZnS photocatalyst under the same reaction conditions (Fig. S16 and S17 in ESI†). The degradation of methylene blue was comparable to that of MO. However, in case of phenolphthalein, the degradation was lower (49% in 60 min) under the identical reaction conditions. This difference in degradation might be due to the difference in redox potentials of different dyes along with their difference in adsorption capacities.

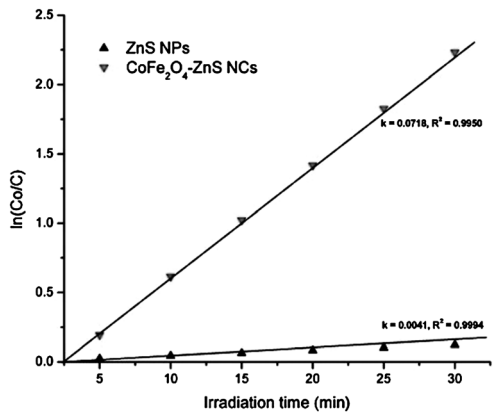

Fig. 7 Kinetics of MO degradation in the presence of ZnS NPs and $CoFe_2O_4$–ZnS NCs.

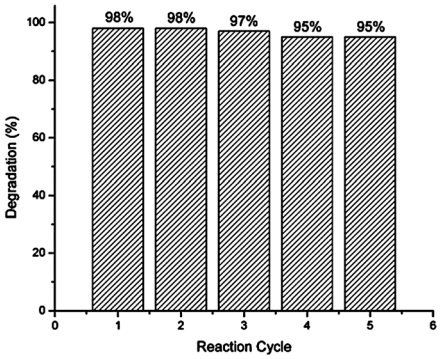

Fig. 8 Recyclability of photocatalytic degradation of MO.

We further observed that the magnetic photocatalyst could be easily separated in the liquid-phase reaction with the aid of an external magnet. To ensure complete removal of the catalyst we measured the energy-dispersive X-ray spectrum of the water residue after centrifugation of the treated water at very high speed and no elemental contribution present in the nanocomposite was detected. The recyclability of the photocatalyst was tested upon separation of the photocatalyst magnetically and then performance of photocatalysis for multiple cycles (Fig. 8). We have not observed any significant loss of activity up to five catalytic cycles, which indicates that the as prepared magnetic photocatalyst is stable and very effective for the removal of organic contaminants from water.

Conclusions

In conclusion, we have developed a $CoFe_2O_4$–ZnS nanocomposite by a facile method. The enhanced photocatalytic activity, easy magnetic separation and multiple reuses make possible the practical utility of the new magnetic nanocomposite in photocatalysis.

Acknowledgements

Financial support from DST (India) (grant no. SR/S1/RFPC- 07/2006 and SR/NM/NS-18/2011) is gratefully acknowledged. The authors would also like to acknowledge the support from IIT Guwahati for analytical facilities *viz*. TEM, VSM, FESEM, XRD and Laser micro-Raman analysis.

Notes and references

1 N. Sounderya and Y. Zhang, *Recent Pat. Biomed. Eng.*, 2008, **1**, 34–42.
2 Y. Ahu, L. P. Stubbs, F. Ho, R. Liu, C. P. Ship, J. A. Maguire and N. S. Hosmane, *ChemCatChem*, 2010, **2**, 365–374.
3 V. P. Kamat, R. Huehn and R. Nicolaescu, *J. Phys. Chem. B*, 2002, **106**, 788–794.
4 R. Y. Hong, J. H. Li, L. L. Chen, D. Q. Liua, H. Z. Li, Y. Zheng and J. Ding, *Powder Technol.*, 2009, **189**, 426–432.
5 J. H. Bang, R. J. Helmich and K. S. Suslick, *Adv. Mater.*, 2008, **20**, 2599–2603.
6 M. R. Hoffimann, S. T. Martin, W. Choi and D. W. Bahnemann, *Chem. Rev.*, 1995, **95**, 69–96.
7 A. Kudo and M. Sekizawa, *Chem. Commun.*, 2000, 1371–1372.
8 I. Tsuji and A. Kudo, *J. Photochem. Photobiol., A*, 2003, **156**, 249–252.
9 C. L. Torres-Martinez, R. Kho, O. I. Mian and R. K. Mehra, *J. Colloid Interface Sci.*, 2001, **240**, 525–532.

10 Y. Wada, H. Yin, T. Kitamura and S. Yanagida, *Chem. Commun.*, 1998, 2683–2684.
11 H. Yin, Y. Wada, T. Kitamura and S. Yanagida, *Environ. Sci. Technol.*, 2001, **35**, 227–231.
12 J. H. Bang, R. J. Helmich and K. S. Suslick, *Adv. Mater.*, 2008, **20**, 2599–2603.
13 S. Yanagida, K. Mizumoto and C. J. Pac, *J. Am. Chem. Soc.*, 1986, **108**, 647–654.
14 S. Yanagida, T. Azuma, Y. Midori, C. J. Pac and H. Sakurai, *J. Chem. Soc. Perkin Trans.*, 1985, **2**, 1487–1493.
15 J. M. Herrmann, F. J. Rivas and R. Montero-de-espinosa, Appl. Catal., *B Environ.*, 1998, **17**, 15–23.
16 D. Beydoun, R. Amal, G. Low and S. McEvoy, *J. Phys. Chem. B*, 2000, **104**, 4387–4396.
17 D. Beydoun, R. Amal, J. Scott, G. Low and S. McEvoy, *Chem. Eng. Technol.*, 2001, **24**, 745–748.
18 S. W. Lee, J. Drwiega, C. Y. Wu, D. Mazyck and W. M. Sigmund, *Chem. Mater.*, 2004, **16**, 1160–1164.
19 F. Chen, Y. D. Xie, J. C. Zhao and G. X. Lu, *Chemosphere*, 2001, **44**, 1159–1168.
20 S. Rana, R. S. Srivastava, M. M. Sorensson and R. D. K. Misra., *Mater. Sci. Eng., B*, 2005, **119**, 144–151.
21 X. U. Shihong, S. Wenfeng, Y. Jian, C. Mingxia and S. Jianwei, *Chin. J. Chem. Eng.*, 2007, **15**, 190–195.
22 Y. Gao, B. H. Chen, H. L. Li and Y. X. Ma, *Mater. Chem. Phys.*, 2003, **80**, 348–355.
23 P. W. Sellwood, *Magnetochemistry*, Interscience, London, 1956.
24 C. Borgohain, K. K. Senapati, D. Mishra, K. C. Sarma and P. Phukan, *Nanoscale*, 2010, **2**, 2250–2256.
25 K. K. Senapati, C. Borgohain, K. C. Sarma and P. Phukan, *J. Mol. Catal. A: Chem.*, 2011, **339**, 24–31.
26 K. K. Senapati, C. Borgohain, K. C. Sarma and P. Phukan, *J. Mol. Catal. A: Chem.*, 2011, **346**, 111–116.
27 K. K. Senapati, S. Roy, C. Borgohain and P. Phukan, *J. Mol. Catal. A: Chem.*, 2012, **352**, 128–134.
28 E. S. Murdock, R. F. Simmons and R. Davidson, *IEEE Trans. Magn.*, 1992, **28**, 3078–3083.
29 G. Zhang, W. Xu, Z. Li, W. Hu and Y. Wang, *J. Magn. Magn. Mater.*, 2009, **321**, 1424–1427.
30 H. A. J. L. Mourao, A. R. Malagutti and C. Ribeiro, *Appl. Catal., A*, 2010, **382**, 284–292.
31 N. Saravanan, G. B. Teh, S. Y. P. Yap and K. M. Cheong, *J. Mater. Sci.: Mater. Electron.*, 2008, **19**, 1206–1208.
32 S. J. Greg and K. S. W. Sing, *Adsorption, Surface Area, and Porosity*, Academic, New York, 1997.
33 X. Ye, Y. Fang, Y. Hu, T. Xia, W. Zhuang and Z. Long, *Mater. Lett.*, 2007, **61**, 5026–5028.
34 X. Cao and L. Gu, *Nanotechnology*, 2005, **16**, 180–185.
35 T. Hyeon, Y. Chung, J. Park, S. S. Lee, Y.-W. Kim and B. H. Park, *J. Phys. Chem. B*, 2002, **106**, 6831–6833.
36 B. D. Cullity, *Elements of X-ray diffraction*, Addison-Wesley Publishing Co. Inc., Reading, MA, 1978, p. 363.
37 P. C. Morias, S. W. da Silva, M. A. G. Soler and N. Baske, *J. Phys. Chem. A*, 2004, **104**, 2894–2896.
38 S. S. Kumar, M. A. Khadar, S. K. Dhara, T. R. Ravindran and K. G. M. Nair, *Nucl. Instrum. Methods Phys. Res., Sect. B*, 2006, **251**, 435–440.
39 Z. W. Wang, R. T. Downs, V. Pischedda, R. Shetty, S. K. Saxena, C. S. Zha and Y. S. Zhao, *Phys. Rev. B: Condens. Matter*, 2003, **68**, 094101.
40 L. Zhang and Z. Li, *J. Alloys Compd.*, 2009, **469**, 422–426.
41 J. Tauc, *Amorphous and liquid semiconductor*, Plenum, London and New York, 1974, p. 159.
42 Z. Jiao, X. Geng, M. Wu, Y. Jiang and B. Zhao, *Colloids Surf., A*, 2008, **313**, 31.
43 J. B. Silva, W. de Brito and N. D. S. Mohallem, *Mater. Sci. Eng., B*, 2004, **112**, 182.
44 L. Ge, *Mater. Chem. Phys.*, 2001, **69**, 7–9.
45 W. Cun, Z. Jincai, W. Xinming, M. Bixian, S. Guoying, P. Ping'an and F. Jiamo, *Appl. Catal., B*, 2002, **39**, 269–179.
46 Y. Yang, Y. Jiang, Y. Wang and Y. Sun, *J. Mol. Catal. A: Chem.*, 2007, **270**, 56–60.
47 A. Fujishima, T. N. Rao and D. A. Tryk, *J. Photochem. Photobiol., C*, 2000, **1**, 1.